Article

Parallel Tempering Monte Carlo Studies of Phase Transition of Free Boundary Planar Surfaces

Andrey Shobukhov (1) **and Hiroshi Koibuchi**(2) *

(1)Faculty of Computational Mathematics and Cybernetics, Lomonosov Moscow State University, 119991, Moscow, Leninskiye Gory, MSU, 2-nd Educational Building, Russia

(2)Department of Industrial Engineering, National Institute of Technology, Ibaraki College, Nakane 866, Hitachinaka, Ibaraki 312-8508, Japan

Abstract: We numerically study surface models defined on hexagonal disks with a free boundary. 2D surface models for planer surfaces have recently attracted interest due to the engineering applications of functional materials such as graphene and its composite with polymers. These 2D composite meta-materials are strongly influenced by external stimuli such as thermal fluctuations if they are sufficiently thin. For this reason, it is very interesting to study the shape stability/instability of thin 2D materials against thermal fluctuations. In this paper, we study three types of surface models including Landau-Ginzburg (LG) and Helfirch-Polyakov models defined on triangulated hexagonal disks using the parallel tempering Monte Carlo simulation technique. We find that the planer surfaces undergo a first-order transition between the smooth and crumpled phases in the LG model and continuous transitions in the other two models. The first-order transition is relatively weaker compared to the transition on spherical surfaces already reported. The continuous nature of the transition is consistent with the reported results, although the transitions are stronger than that of the reported ones.

Keywords: soft biological materials; stress-strain diagram; J-shaped diagram; Monte Carlo; statistical mechanics; Finsler geometry

1. Introduction

The two-dimensional surface model proposed by Helfrich is a model for biological membranes composed of lipid molecules, and it shares almost the same mathematical structure with the Polyakov's rigid string model for elementary particles in subatomic scales [1,2]. In those models, the extrinsic curvature or bending energy plays an essential role in maintaining the smooth shape of surfaces, and because of its mathematical transparency, a lot of studies are conducted on the phase structure of the model between the smooth and crumpled phases [3–9]. The discrete surface models defined on triangulated lattices have also been extensively studied by Monte Carlo (MC) simulations [13–19].

However, the order of the crumpling transition is still controversial. Since the discrete model depends on the discretization of continuous Hamiltonian, we have a variety of discrete models [20,21]. Indeed, the curvature energy itself has a lot of variation such as extrinsic and intrinsic curvatures. For almost all these discrete models, MC studies predict that the models undergo a first-order crumpling transition if the lattice is of spherical topology and allowed to self-intersect (⇔ self-intersecting) [20]. Here, we should note that only self-intersecting and fixed-connectivity lattice models are studied in this paper, and self-avoiding models and fluid surface models are out of consideration [15,16]. Intrinsic curvature models have also a first-order crumpling transition even on a disk surface [21], and the intrinsic curvature models are also out of consideration in this paper. The first-order crumpling transition is supported by theoretical studies on the basis of non-perturbative renormalization group

Peer-reviewed version available at Polymers 2018, 10, 1360; doi:10.3390/polym10121360

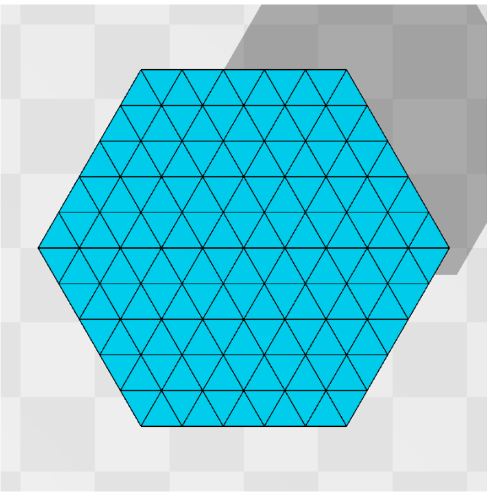

Figure 1. A hexagonal lattice discretized by regular triangles. The total number of vertices N including those on the boundary is given by $N\!=\!91$. This number is calculated by the formula $N\!=\!3L^2\!+\!3L\!+\!1$, where $L(\!=\!5)$ is the number of division of the edge of original hexagon. This type of hexagonal lattice is used to define discrete Hamiltonians of the surface models studied in this paper.

techniques [8,9]. In contrast, it is reported that the order of transition is of second-order on the free boundary lattices [22,23]. Therefore, this continuous transition combining the above mentioned first-order one indicates that the order of transition depends on the surface topology; spheres or free boundary planer disks.

In this paper, we study three different surface models by the parallel tempering MC (PTMC) technique to check whether the transition is of second-order or not on triangulated disks with free boundary. The PTMC technique was developed to simulate the spin glass models at very low temperature, where the standard Metropolis MC technique is not effective [24,25]. It is also reported that this PTMC technique can be applied to phenomena which undergo first-order transitions [26,27]. Therefore, we expect that the PTMC technique can also be used to study the phase structure of the surface models in this paper even if these models have first-order transitions [28].

We should comment on the reason why the crumpling transition is interesting. Indeed, graphite oxide sheets in solvents have a crumpled state [29,30]. Crumpled states can also be observed in graphenes [31,32]. The surface condition of graphenes is altered by corrugations, and therefore ripples, wrinkles and crumples emerge [33,34]. These surface states modify or enhance the material properties such as mechanical, electrical and optical ones [35]. The crumpled graphene, for example, is expected to have enhanced chemical activities and energy storage capacities [36]. In addition to pure graphenes, polymer-graphene nano-composite or graphene-based polymers (or polymer-based graphenes) also has the crumpled states [37–40]. For the application of crumpled states of these graphene-based materials, it is interesting to study their stability against thermal fluctuation or some other stimuli in environmental conditions [41]. Therefore, the crumpled state is worthwhile studying in terms of phase transition.

2. Models and Monte Carlo Technique

2.1. Triangulated Disk

Discrete surface models are defined on such a triangulated disk shown in Fig. 1. The lattice is characterized by the numbers (N, N_E, N_T), which are the total number of vertices, the total number of edges, and the total number of triangles. Using the number L of division of the hexagon edge, we have the expressions for these numbers such that $(N, N_E, N_T)\!=\!(3L^2\!+\!3L\!+\!1, 9L^2\!+\!3L, 6L^2)$. The lattice shown in Fig.1 is obtained by $L = 5$, and hence $(N, N_E, N_T) = (91, 240, 150)$. We chose a sufficiently small L to visualize the lattice structure. The lattices used in the simulations are larger than the lattice in Fig. 1. The lattice spacing a for the edge length can be used as the length scale [42]. However, the simulation data are not directly compared to the experimental ones in this paper, and for this reason we fix a to $a = 1$ for simplicity.

2.2. Landau-Ginzburg surface Model

The so-called Landau-Ginzburg surface model is first introduced and studied by Paczuski, Kardar and Nelson in [43], and this model is also numerically studied in [44]. Let $\mathbf{r}(\in \Re^3)$ be the surface position. The continuous Hamiltonian is given by

$$S_{\rm LG}(\mathbf{r}) = \frac{t}{2}\int d^2x \,(\partial_a \mathbf{r})^2 + \frac{\kappa}{2}\int d^2x \left(\partial^2 \mathbf{r}\right)^2 + u\int d^2x \,(\partial_a \mathbf{r}\cdot\partial_b \mathbf{r})^2 + v\int d^2x \,(\partial_a \mathbf{r}\cdot\partial_a \mathbf{r})^2, \qquad (1)$$

where $\partial_a \mathbf{r} = \partial \mathbf{r}/\partial x_a$, $(a = 1, 2)$ is a tangential vector along the local coordinate axis x_a on the surface and plays a role of the order parameter. The real numbers t, κ, u, v are the coefficients of the energy terms, which are square and quadratic with respect to $\partial_a \mathbf{r}$. The second term is defined by the square of second-order differentials $(\partial^2 \mathbf{r})^2$.

The continuous energy $S_{\rm LG}(\mathbf{r})$ in Eq. (1) can be written more explicitly such that

$$\begin{aligned}
&S_{\rm LG} = tS_1 + \kappa S_2 + uS_3 + vS_4,\\
&S_1 = \frac{1}{2}\int d^2x \left[(\partial_1 \mathbf{r})^2 + (\partial_2 \mathbf{r})^2\right],\\
&S_2 = \frac{1}{2}\int d^2x \left(\partial_1^2 \mathbf{r} + \partial_2^2 \mathbf{r}\right)^2 = \frac{1}{2}\int d^2x \left(\partial_1^2 \mathbf{r}\cdot\partial_1^2 \mathbf{r} + \partial_2^2 \mathbf{r}\cdot\partial_2^2 \mathbf{r} + 2\partial_1^2 \mathbf{r}\cdot\partial_2^2 \mathbf{r}\right),\\
&S_3 = \int d^2x \left[(\partial_1 \mathbf{r}\cdot\partial_1 \mathbf{r})^2 + (\partial_2 \mathbf{r}\cdot\partial_2 \mathbf{r})^2 + 2\,(\partial_1 \mathbf{r}\cdot\partial_2 \mathbf{r})^2\right],\\
&S_4 = \int d^2x \left[(\partial_1 \mathbf{r}\cdot\partial_1 \mathbf{r})^2 + (\partial_2 \mathbf{r}\cdot\partial_2 \mathbf{r})^2 + 2\,(\partial_1 \mathbf{r})^2\,(\partial_2 \mathbf{r})^2\right].
\end{aligned} \qquad (2)$$

The detailed information on the role of each term is written in Ref. [44], and we briefly describe the outline of each term. The first term S_1 is given by the integration of length squares of the tangential vectors, and it simply plays a role of the tensile energy. The second term S_2 plays a role of the bending energy and the in-plane shear energy, and the third term S_3 contains both the tensile and the shear energy components. The final term S_4 is a quadratic tensile energy term.

The discrete Hamiltonian is as follows [44]:

$$\begin{aligned}
&S_{\rm LG} = tS_1 + \kappa S_2 + uS_3 + vS_4,\\
&S_1 = \frac{2}{3}\sum_{ij}\left(\mathbf{r}_i - \mathbf{r}_j\right)^2 = \frac{2}{3}\sum_{i}\mathbf{e}_i^2,\\
&S_2 = \frac{1}{3}\sum_{ij}\left(\mathbf{e}_i - \mathbf{e}_j\right)^2 + \frac{1}{3}\sum_{(ij),(kl)}\left(\mathbf{e}_i - \mathbf{e}_j\right)\cdot\left(\mathbf{e}_k - \mathbf{e}_l\right),\\
&S_3 = \frac{2}{3}\sum_{\Delta}\left[\left(\mathbf{e}_1^2\right)^2 + \left(\mathbf{e}_2^2\right)^2 + \left(\mathbf{e}_3^2\right)^2 + (\mathbf{e}_1\cdot\mathbf{e}_2)^2 + (\mathbf{e}_2\cdot\mathbf{e}_3)^2 + (\mathbf{e}_3\cdot\mathbf{e}_1)^2\right],\\
&S_4 = \frac{2}{3}\sum_{\Delta}\left[\left(\mathbf{e}_1^2\right)^2 + \left(\mathbf{e}_2^2\right)^2 + \left(\mathbf{e}_3^2\right)^2 + \left(\mathbf{e}_1^2\right)\left(\mathbf{e}_2^2\right) + \left(\mathbf{e}_2^2\right)\left(\mathbf{e}_3^2\right) + \left(\mathbf{e}_3^2\right)\left(\mathbf{e}_1^2\right)\right], \qquad ({\rm LG}).
\end{aligned} \qquad (3)$$

Peer-reviewed version available at Polymers 2018, 10, 1360; doi:10.3390/polym10121360

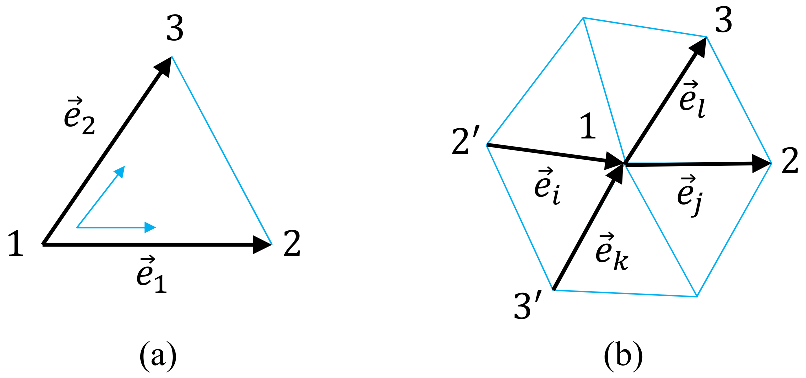

(a) (b)

Figure 2. (a) A local coordinate on a triangle 123 and the edge vectors $\mathbf{e}_1$ and $\mathbf{e}_2$ along the coordinates axes x_1 and x_2. A local coordinate for the discretization of the second-order differential $\partial^2\mathbf{r}$ in S_2 of LG model on (b) a vertex of coordination number $q=6$ (hexagonal).

We briefly summarize how to obtain the discrete Hamiltonian in Eq. (3) from the continuous one in Eq. (2). First of all, we note that the local coordinate origin of the triangle 123 in Fig. 2(a) is at the vertex 1, and hence the differentials $\partial_1\mathbf{r}$ and $\partial_2\mathbf{r}$ in S_1 of Eq. (2) are replaced by

$$\partial_1\mathbf{r} \to \mathbf{e}_1 = \mathbf{r}_2 - \mathbf{r}_1, \quad \partial_2\mathbf{r} \to \mathbf{e}_2 = \mathbf{r}_3 - \mathbf{r}_1. \tag{4}$$

Recalling that there are two other local coordinate origins on the triangle 123, and including all possible terms for the differentials $\partial_1\mathbf{r}$ and $\partial_2\mathbf{r}$ and with the factor $1/3$, we have

$$S_1 = \frac{1}{3}\sum_{\mathit{\Delta}}\left(\mathbf{e}_1^2 + \mathbf{e}_2^2 + \mathbf{e}_3^2\right), \tag{5}$$

where $\mathbf{e}_3 (= \mathbf{r}_3 - \mathbf{r}_2)$ is not written in Fig. 2(a). The integration $\int d^2x$ is replaced by the sum over triangles $\mathit{\Delta}$ such that $\int d^2x \to \sum_{\mathit{\Delta}}$. By replacing the summation convention from the sum over triangles $\sum_{\mathit{\Delta}}$ to the sum over bonds $\sum_i$, we have S_1 in Eq. (3). We should note that this energy S_1 is also defined on the triangles of the boundary.

The second order derivative such as $\partial_1^2\mathbf{r}$ in S_2 is replaced by $\partial_1^2\mathbf{r} \to \mathbf{e}_j - \mathbf{e}_i$ using the vectors $\mathbf{e}_j$ and $\mathbf{e}_i$ on the hexagon in Fig. 2(b), because $\mathbf{e}_j$ and $\mathbf{e}_i$ are considered as the discretization of $\partial_1\mathbf{r}$ along the coordinate axis 2'12 corresponding to the local coordinate axis x_1 at the vertex 1. Another diagonal line 3'13 on this hexagon is considered as the x_2 axis, and thereby the square of Laplacian $(\partial^2\mathbf{r})^2 = (\partial_1^2\mathbf{r} + \partial_2^2\mathbf{r})^2$ is replaced by $(\mathbf{e}_j - \mathbf{e}_i)^2 + (\mathbf{e}_l - \mathbf{e}_k)^2 + 2(\mathbf{e}_j - \mathbf{e}_i)\cdot(\mathbf{e}_l - \mathbf{e}_k)$ using the vectors $\mathbf{e}_i$, $\mathbf{e}_j$,$\mathbf{e}_k$ and $\mathbf{e}_l$ in Fig. 2(b). Thus, we have S_2 in Eq. (3) as a discrete bending energy corresponding to the continuous one $(1/2)\int dx^2 (\partial^2\mathbf{r})^2$ in Eq. (3). The reason for the factor $1/3$ in the discrete expression is because every vertex inside the boundary is assumed to be the center of hexagon, and therefore the summation is triply duplicated. Strictly speaking, the duplication at the vertices close to the boundary is not triple, however, the coefficient is not so important and is simply fixed to $1/3$, which is the same as in the spherical model [44]. In the discrete S_2, $\sum_{ij}$ denotes the sum over the three different diagonal lines, and $\sum_{(ij),(kl)}$ denotes the sum over the corresponding local coordinates on the hexagon.

Note that on the hexagonal lattice, such as shown in Fig. 1, the coordination number at the vertices inside the boundary is given by $q=6$, where the coordination number q_i is the total number of bonds emanating from the vertex i. This is in sharp contrast to spherical lattices, which must include the vertices with $q \neq 6$. Therefore, the vertex with $q=6$ in Fig. 2(b) is sufficient for the discretization of $(\partial^2\mathbf{r})^2$ for all internal vertices. On the boundary vertices, the definition of energy S_2 is slightly different from that on the internal vertices. On the vertices with $q=4$, the square of Laplacian $(\partial^2\mathbf{r})^2 = (\partial_1^2\mathbf{r} + \partial_2^2\mathbf{r})^2$ is

Preprints (www.preprints.org) | NOT PEER-REVIEWED | Posted: 26 October 2018 doi:10.20944/preprints201810.0626.v1

Peer-reviewed version available at Polymers 2018, 10, 1360; doi:10.3390/polym10121360

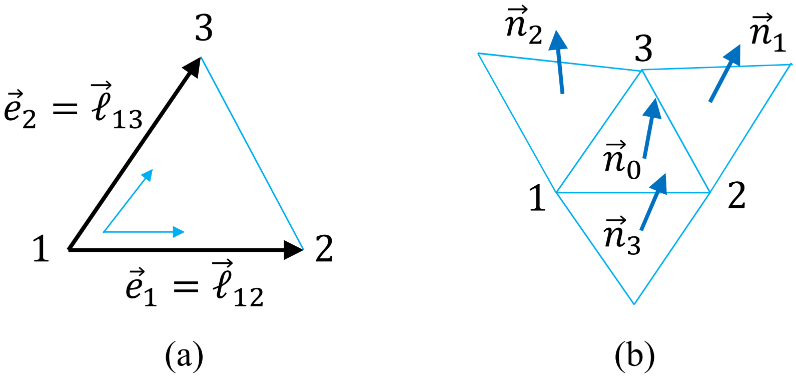

Figure 3. Lattice structure for discretization of the canonical surface model. (a) A local coordinate on the triangle 123 with the edge vectors $\vec{\ell}_{12}$ and $\vec{\ell}_{13}$, and (b) the triangle 123 and its three nearest-neighbor triangles, where the normal vector $\mathbf{n}_0$ interacts with $\mathbf{n}_i(i=1,2,3)$. The local coordinate in (a) is exactly same as that in Fig. 2(a).

simply replaced by $(\mathbf{e}_j-\mathbf{e}_i)^2$ instead of $(\mathbf{e}_j-\mathbf{e}_i)^2+(\mathbf{e}_l-\mathbf{e}_k)^2+2(\mathbf{e}_j-\mathbf{e}_i)\cdot(\mathbf{e}_l-\mathbf{e}_k)$. Moreover, the bending energy S_2 is not defined on the vertices with $q=3$ on the boundary (see Fig. 1).

In the continuous S_3 and S_4 of Eq. (2), the derivatives $\partial_1\mathbf{r}$ and $\partial_2\mathbf{r}$ are replaced by $\mathbf{e}_1$ and $\mathbf{e}_2$ in Eq. (4) on the triangle in Fig. 2(a). The discretization technique is exactly same as the one assumed in S_1, and hence we have the discrete energies S_3 and S_4 in Eq. (3).

The partition function Z is given by the multiple integrations of the vertex positions such that

$$Z = \int^{\prime} \prod_i d\mathbf{r}_i \exp\left(-S_{\rm LG}\right), \tag{6}$$

where the prime in $\int^{\prime}\prod_i d\mathbf{r}_i$ denotes that the center of the mass of surface is fixed at the origin of $\Re^3$.

From the scale invariance of Z, we have

$$\langle S_1^{\prime}\rangle/N = 3/2, \qquad S_1^{\prime} = tS_1+\kappa S_2+2uS_3+2vS_4, \tag{7}$$

where $\langle Q\rangle$ is defined by $\langle Q\rangle=\int^{\prime}\prod_i d\mathbf{r}_i\, Q\,\exp\left(-S_{\rm LG}\right)/Z$ [7,44]. This relation in Eq. (7) can be used to check whether the simulation is correctly performed or not.

2.3. Canonical Model

We start with the continuous form of Hamiltonian $S(\mathbf{r},g)$ of the canonical model, which is defined by a mapping $\mathbf{r}$ from a two-dimensional surface M to the three-dimensional Euclidean space $\Re^3$, such that

$$\mathbf{r}: M \ni (x_1,x_2) \longmapsto \mathbf{r}(x_1,x_2) = (X,Y,Z) \in \Re^3. \tag{8}$$

The variable $\mathbf{r}$, which is originally used to denote the surface position in $\Re^3$, is now used for the symbol of the mapping. Another variable denoted by g in $S(\mathbf{r},g)$ is the metric function g_{ab} on M, where g_{ab} is a 2×2 matrix. The metric g_{ab} originally is not a variable but is determined by a local coordinate, which is fixed arbitrarily by hand from the reparametrization invariance. This invariance is a symmetry of the model under 2D coordinate transformations on the surface $\mathbf{r}(M)$ in $\Re^3$. Thus, the model is slightly extended from the original one in the sense that g_{ab} is a variable that should be physically determined.

Peer-reviewed version available at *Polymers* **2018**, *10*, 1360; doi:10.3390/polym10121360

As a consequence, we have a possibility to obtain surfaces which cannot be in $\Re^3$ in the extended model, whether this is meaningful or not. For example, let us consider the metric

$$g_{ab} = \begin{pmatrix} \ell_{12}^2 & \ell_{12}\ell_{13}\cos\Phi \\ -\ell_{12}\ell_{13}\cos\Phi & \ell_{13}^2 \end{pmatrix} \tag{9}$$

on a surface discretized by piece-wise linear triangles such as in Fig. 3(a), where $\cos\Phi$ is not always identical to $\cos\phi = \vec{\ell}_{12}\cdot\vec{\ell}_{13}/\ell_{12}\ell_{13}$ between the edge vectors $\vec{\ell}_{12}$ and $\vec{\ell}_{13}$ [45]. If $\Phi = \phi$ for all triangles, then this metric is identical with the discrete induced metric $g_{ab} = \mathbf{e}_a\cdot\mathbf{e}_b$. However, if the angles $\{\Phi\}$ do not satisfy the triangle equality, i.e., the sum of three internal angles is not always equal to π, then the surface with such metric in Eq. (9) generally cannot be realized in $\Re^3$.

The continuous Hamiltonian is given by

$$S(\mathbf{r}, g) = \gamma \int_M \sqrt{g}\, d^2x\, g^{ab}\partial_a\mathbf{r}\cdot\partial_b\mathbf{r} + \frac{\kappa}{2}\int_M \sqrt{g}\, d^2x\, g^{ab}\partial_a\mathbf{n}\cdot\partial_b\mathbf{n}, \quad (\gamma = 1) \tag{10}$$

where the surface tension coefficient γ is always fixed to $\gamma = 1$. The symbol g^{ab} denotes the inverse of g_{ab}, and g is its determinant. We should note that g_{ab} assumed in the expression of $S(\mathbf{r}, g)$ in Eq. (10) is a variable that should be determined just like the mapping $\mathbf{r}$ as mentioned above [46]. Note also that this Hamiltonian is a two-dimensional extension of the polymer model of Doi-Edwards [47].

Here, we should note that the real surface $\mathbf{r}(M)$ in $\Re^3$ corresponding to the material under consideration is described by the induced metric $g_{ab} = \partial_a\mathbf{r}\cdot\partial_b\mathbf{r}$. This allows us to consider that the surface with a given metric g_{ab} is different from the real surface, pointing to the possibility for the surface to correspond to this g_{ab}. Therefore, from this set of surfaces, a physically meaningful surface should be uniquely determined by the modeling. For this reason, we introduce a two-dimensional surface M in addition to the real surface with $\partial_a\mathbf{r}\cdot\partial_b\mathbf{r}$, both of which should be physically determined. This is another extension of the surface model, and this is the meaning of the mapping described in Eq. (8). Note that the surface M is not necessarily a manifold [45,48,49].

The problem is how to determine g_{ab} for M. One possible and simple technique is to fix g_{ab} to the Euclidean metric such that $g_{ab} = \delta_{ab}$. In this case, M is a simple two-dimensional Euclidean space and plays no role in describing the model, however, we use M to express the domain in the two-dimensional integrations in $S(\mathbf{r})$. Thus, the only variable to be determined is $\mathbf{r}$, and $S(\mathbf{r})$ is now given by

$$S(\mathbf{r}) = \gamma \int_M d^2x\, \partial_a\mathbf{r}\cdot\partial_a\mathbf{r} + \frac{\kappa}{2}\int_M d^2x\, \partial_a\mathbf{n}\cdot\partial_a\mathbf{n}, \quad (\gamma = 1). \tag{11}$$

One simple reason for why we assume the Euclidean metric δ_{ab} for g_{ab} is as follows: The Hamiltonian in Eq. (10) is invariant under an arbitrary conformal transformation $g_{ab} \to g'_{ab} = f(x)g_{ab}$ with a positive function $f(x)$ on M. This invariance is described by $S(\mathbf{r}, g) = S(\mathbf{r}, g')$ and implies that the metric g_{ab} can be chosen relatively freely, and therefore it is fixed to the simplest one such that $g_{ab} = \delta_{ab}$.

The discrete Hamiltonians are obtained from the continuous one in Eq. (11) by the replacement of the differentials in Eq. (4). Here, we use the symbols $\vec{\ell}_{12} = \mathbf{e}_1$ and $\vec{\ell}_{13} = \mathbf{e}_2$ for the edge vectors (Fig. 3(a)), and $\ell_{ij} = |\vec{\ell}_{ij}| = |\mathbf{r}_j - \mathbf{r}_i|$ for the edge (or bond) length. Thus, we obtain

$$\begin{aligned} &S(\mathbf{r}) = S_1 + \kappa S_2, \\ &S_1 = \sum_{(i,j)}\left(\mathbf{r}_i - \mathbf{r}_j\right)^2 = \sum_{(i,j)}\ell_{ij}^2, \quad S_2 = \sum_{(i,j)}\left(1 - \mathbf{n}_i\cdot\mathbf{n}_j\right), \qquad (\text{cano}), \end{aligned} \tag{12}$$

where the factor $4/3$ is eliminated from both S_1 and S_2 for simplicity. This S_1 is exactly the same as S_1 of the LG model in Eq. (3) up to the numerical factor. The symbol $\sum_{(ij)}$ in S_1 denotes the sum over all bonds (ij) connecting the vertices i and j. In contrast, (ij) in the sum $\sum_{(ij)}$ of S_2 denotes the triangles sharing a common bond (Fig. 3(b)), and the unit normal vector $\mathbf{n}_i$ is defined on the triangle i. The

Peer-reviewed version available at Polymers 2018, 10, 1360; doi:10.3390/polym10121360

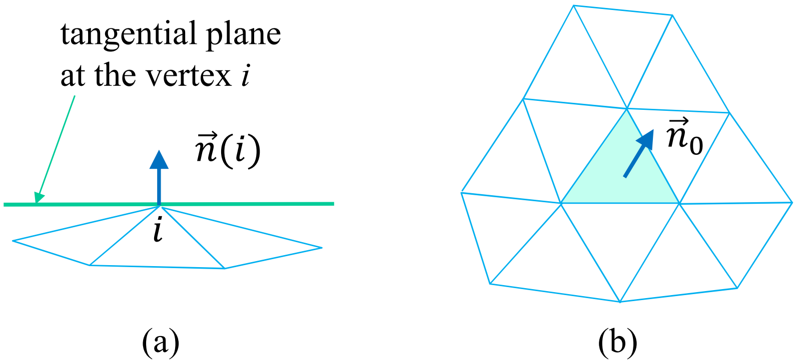

Figure 4. Lattice structure for discretization of the modified canonical surface model. (a) The tangential plane at the vertex i and its normal vector $\mathbf{n}(i)$, and (b) a triangle and its neighboring triangles, where the normal vector $\mathbf{n}_0$ interacts with those of the neighboring triangles. The range of interaction is slightly larger than that shown in Fig. 3(b).

partition function of the canonical model is exactly the same as Z in Eq. (6) for LG model except the Hamiltonian in the Boltzmann factor.

2.4. Modified Canonical Model

The third model, which we call “modified canonical model”, is obtained from the same continuous Hamiltonian in Eq. (11) assumed for the canonical model. The only difference is a discretization of the bending energy S_2, where the unit normal vector $\mathbf{n}(i)$ at the vertex i (Fig. 4(a)) is used as well as the normal vector $\mathbf{n}_i$ on the triangle i (Fig. 3(b)). The discrete Hamiltonian is given by [45]

$$\begin{aligned} &S(\mathbf{r}) = S_1 + \kappa S_2, \\ &S_1 = \sum_{(i,j)} \ell_{ij}^2, \quad S_2 = \sum_{i=1}^{N} \sum_{j(i)} \left[1 - \mathbf{n}(i) \cdot \mathbf{n}_{j(i)}\right], \qquad (\mathrm{modi}), \end{aligned} \tag{13}$$

where $\mathbf{n}_{j(i)}$ in S_2 is the unit normal vector of the triangle $j(i)$ connected to the vertex i. The normal vector $\mathbf{n}(i)$ at the vertex i is defined by (Fig. 4(a))

$$\mathbf{n}(i) = \mathbf{N}_i/|\mathbf{N}_i|, \quad \mathbf{N}_i = \sum_{j(i)} \mathbf{n}_{j(i)} A_{j(i)}, \tag{14}$$

where $A_{j(i)}$ is the area of the triangle $j(i)$. Note that the interaction range of the normal vectors $\mathbf{n}_i$ is slightly larger than that of the canonical model (Fig. 4(b)). In fact, only two nearest neighbor vectors $\mathbf{n}_i$ and $\mathbf{n}_j$ are directly coupled in S_2 in Eq. (12) of the canonical model, and as a consequence only three nearest neighbor vectors $\mathbf{n}_i (i = 1, 2, 3)$ are coupled to $\mathbf{n}_0$ (see Fig. 3(b)). In contrast, as shown in Fig. 4(b), the non-nearest neighbor $\mathbf{n}_i$ and $\mathbf{n}_j$, of which the triangles i and j do not directly contact each other, are coupled to $\mathbf{n}_0$ in S_2 in Eq. (13) of the modified model.

2.5. Parallel tempering Monte Carlo technique

The so-called parallel tempering Monte Carlo (PTMC) technique developed for the spin glass model at low temperatures is successfully applied to the first-order crumpling transition of the canonical model on spherical lattices [28]. In this subsection, the outline of the PTMC technique applied to the tethered surface model is briefly presented.

Let $(\mathbf{r}, \kappa)$ represent a system of configuration $\mathbf{r}(= \{\mathbf{r}_1, \mathbf{r}_2, \cdots, \mathbf{r}_N\})$ with a given κ, which is assumed to be changed. In the case of LG model, the parameter κ is also changed while the other

Peer-reviewed version available at Polymers 2018, 10, 1360; doi:10.3390/polym10121360

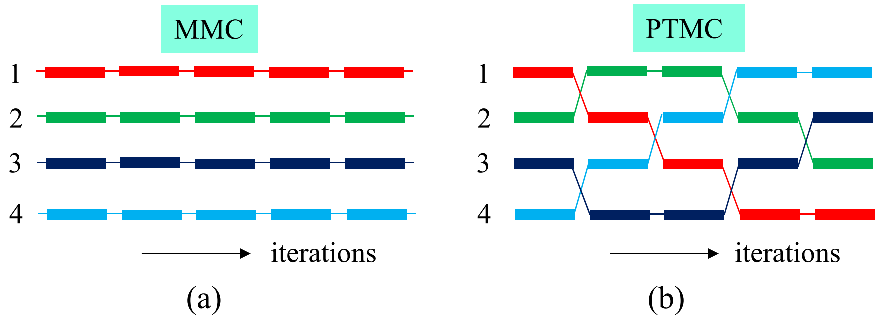

Figure 5. Illustration of how the replica systems evolve in (a) MMC and (b) PTMC simulations. In (a) MMC simulations, each system evolves independent of the other systems, while in (b) PTMC simulations, the systems are exchanged.

three parameters (t, u, v) are fixed in the simulations in this paper. In this PTMC, N_R replicas $\{(\mathbf{r}_1, \kappa_1), (\mathbf{r}_2, \kappa_2), \cdots, (\mathbf{r}_{N_R}, \kappa_{N_R})\}$ are simulated in parallel by the standard Metropolis MC (MMC) simulation technique [50,51], and the systems are exchanged after sufficiently long MMC runs. Because of this exchange, the total number of different combinations $\{(\mathbf{r}_1, \kappa_1), (\mathbf{r}_2, \kappa_2), \cdots, (\mathbf{r}_{N_R}, \kappa_{N_R})\}$ is $N_R!$.

The N_R replicas are updated as follows:

- (P_1) Perform long MMC simulations for N_R replicas
- (P_2) Exchange all nearest neighbor systems $(\mathbf{r}, \kappa)$ and $(\mathbf{r}', \kappa')$ with the probability

$$W(\mathbf{r}, \kappa|\mathbf{r}', \kappa') = \mathrm{Min}\left[1, \exp(-\Delta)\right], \quad \Delta = (\kappa' - \kappa)\left[S_2(\mathbf{r}) - S_2(\mathbf{r}')\right] \tag{15}$$

- (P_3) Repeat P_1 and P_2

We should note that the process P_1 can be performed in parallel as mentioned above. In the exchange process P_2, only bending energy S_2 is used, and no information on the other energy S_1 is used in the canonical and modified canonical models. This is also true for the LG model, and no information on the energies S_1, S_3 and S_4 is left out in the exchange process.

Figures 5(a) and 5(b) intuitively show the difference of MMC and PTMC simulations for four replica systems. The numbers $1, 2, 3, 4$ denote the bending rigidities such as $\kappa_1, \cdots, \kappa_4$, and the color blocks denote the configurations $\mathbf{r}_1, \cdots, \mathbf{r}_4$. The combination of $(\mathbf{r}_i, \kappa_j)$ is exchanged as the iterations evolve in the PTMC simulation.

Here, we briefly show that all micro states $\{\mathbf{r}, \kappa\}$ satisfy the canonical Boltzmann distribution as a result of PTMC simulations. Let $P(\{\mathbf{r}, \kappa\})$ be a probability distribution for all the states $\{\mathbf{r}, \kappa\}$ such that

$$P(\{\mathbf{r}, \kappa\}) = \prod_{m=1}^{N_R} P_{\mathrm{eq}}(\mathbf{r}_m, \kappa_m), \quad P_{\mathrm{eq}}(\mathbf{r}, \kappa) = Z^{-1} \exp\left[-S(\mathbf{r}, \kappa)\right], \quad S(\mathbf{r}, \kappa) = \bar{S}(\mathbf{r}) + \kappa S_2(\mathbf{r}), \tag{16}$$

where $\bar{S}(\mathbf{r})$ is independent of κ and given by $\bar{S}(\mathbf{r}) = tS_1(\mathbf{r}) + uS_3(\mathbf{r}) + vS_4(\mathbf{r})$ for the LG model and $\bar{S}(\mathbf{r}) = S_1(\mathbf{r})$ for the other two models. The $P_{\mathrm{eq}}(\mathbf{r}, \kappa)$ in Eq. (16) is the Boltzmann distribution function of the state $(\mathbf{r}, \kappa)$. If the PTMC exchange satisfies the detailed balance condition described by

$$P(...,;\mathbf{r}, \kappa; ...; \mathbf{r}', \kappa'; ...)W(\mathbf{r}, \kappa|\mathbf{r}', \kappa') = P(...,;\mathbf{r}', \kappa; ...; \mathbf{r}, \kappa'; ...)W(\mathbf{r}', \kappa|\mathbf{r}, \kappa'), \tag{17}$$

then we understand from the well-known uniqueness theorem that this P is the uniquely determined probability [28]. Note that the right-hand side of Eq. (17) is obtained from the left-hand side by exchanging $\mathbf{r}$ and $\mathbf{r}'$. Thus, we should prove that $P(\{\mathbf{r}, \kappa\})$ in Eq. (16) satisfies the condition in Eq. (17).

This can be accomplished in two steps. The first step is to see that Eq. (17) for $P(\{\mathbf{r},\kappa\})$ in Eq. (16) is equivalent with the relation

$$\frac{W(\mathbf{r},\kappa|\mathbf{r}',\kappa')}{W(\mathbf{r}',\kappa|\mathbf{r},\kappa')} = \exp\left(-\Delta\right) \tag{18}$$

under the condition given by Eq. (15). The second step is to see that the relation in Eq. (18) is correct. This second step is almost trivial from the definitions of $W(\mathbf{r},\kappa|\mathbf{r}',\kappa')$ and Δ in Eq. (15). The first step is also straightforward to prove.

The assumed parameters for the simulations including the total number of MC sweeps (MCS) are listed in Table 1, where 1 MCS consists of the processes P_1 and P_2 of PTMC. In Table 1, the symbol N is the total number of vertices, #total (MCS) and #therm (MCS) are the total number of MCS and the total number of thermalization MCS, and n_{P_1} denotes the number of iterations performed in P_1 per 1 MC sweep. This n_{P_1} is fixed to $n_{P_1}=10$ (or $n_{P_1}=20$), and this implies that the total number of MMC (including thermalization) iterations for each replica is 10 (or 20) times larger than the #total (MCS). The N_R is the total number of replicas, and κ_1 and κ_{N_R} ($\kappa_1 < \kappa_{N_R}$) are the bending rigidity of the replica 1 and N_R, $\mathit{\Delta}\kappa (= (\kappa_{N_R}-\kappa_1)/N_R)$ is the difference of κ between two neighboring replicas, which will be exchanged in the process P_2. The total number of iterations #total for the large lattices in the latter two models is not so large compared to those for smaller lattice in the LG model.

Table 1. The parameters assumed for the simulations; n_{P_1} denotes the total number of MMC iterations performed in the P_1 process per 1 MCS for each replica, κ_1 and κ_{N_R} ($\kappa_1 < \kappa_{N_R}$) are the bending rigidity of the replica 1 and N_R, and $\mathit{\Delta}\kappa (= (\kappa_{N_R}-\kappa_1)/N_R)$ is the difference of κ between two neighboring replicas.

Model	N	#total (MCS)	#therm (MCS)	n_{P_1}	N_R	κ_1	κ_{N_R}	$\mathit{\Delta}\kappa$
LG	7351	2.5×10^{8}	2.5×10^{7}	10	24	0.1835	0.187	1.46×10^{-4}
LG	5677	2.5×10^{8}	2.5×10^{7}	10	24	0.1842	0.1878	1.5×10^{-4}
LG	4219	9×10^{7}	3×10^{7}	10	24	0.183	0.194	4.58×10^{-4}
LG	2611	1×10^{7}	2×10^{6}	10	24	0.18	0.2	8.33×10^{-4}
cano	44287	3.8×10^{7}	1.8×10^{7}	20	24	0.766	0.782	2.5×10^{-4}
cano	30907	8×10^{7}	3×10^{7}	20	24	0.764	0.787	9.58×10^{-4}
cano	20917	1×10^{8}	1.5×10^{7}	20	24	0.762	0.792	1.25×10^{-3}
cano	12097	7.5×10^{7}	7.5×10^{6}	10	24	0.77	0.804	1.42×10^{-3}
modi	20917	6.4×10^{7}	1×10^{7}	20	24	0.451	0.467	6.67×10^{-4}
modi	12097	1.9×10^{8}	2.5×10^{7}	10	24	0.448	0.47	9.167×10^{-4}
modi	7351	5×10^{8}	5×10^{7}	10	16	0.444	0.476	2×10^{-2}
modi	4219	5×10^{8}	1.5×10^{7}	10	16	0.44	0.49	6.96×10^{-2}

3. Simulation results

3.1. Snapshots

Firstly, in the presentation section, we show snapshots, which are obtained as one of the configurations from the replicas $i=1$ and $i=N_R$ in each model. In the upper (lower) low in Fig. 6, the snapshots are obtained from the replica $i=N_R$ ($i=1$) of the (a) LG, (b) canonical, and (c) modified canonical models. The size of lattices are the largest for these snapshots, and hence from Table 1 all N_R are given by $N_R=24$. From Table 1, we find that the values of κ corresponding to these replicas are

Peer-reviewed version available at Polymers **2018**, 10, 1360; doi:10.3390/polym10121360

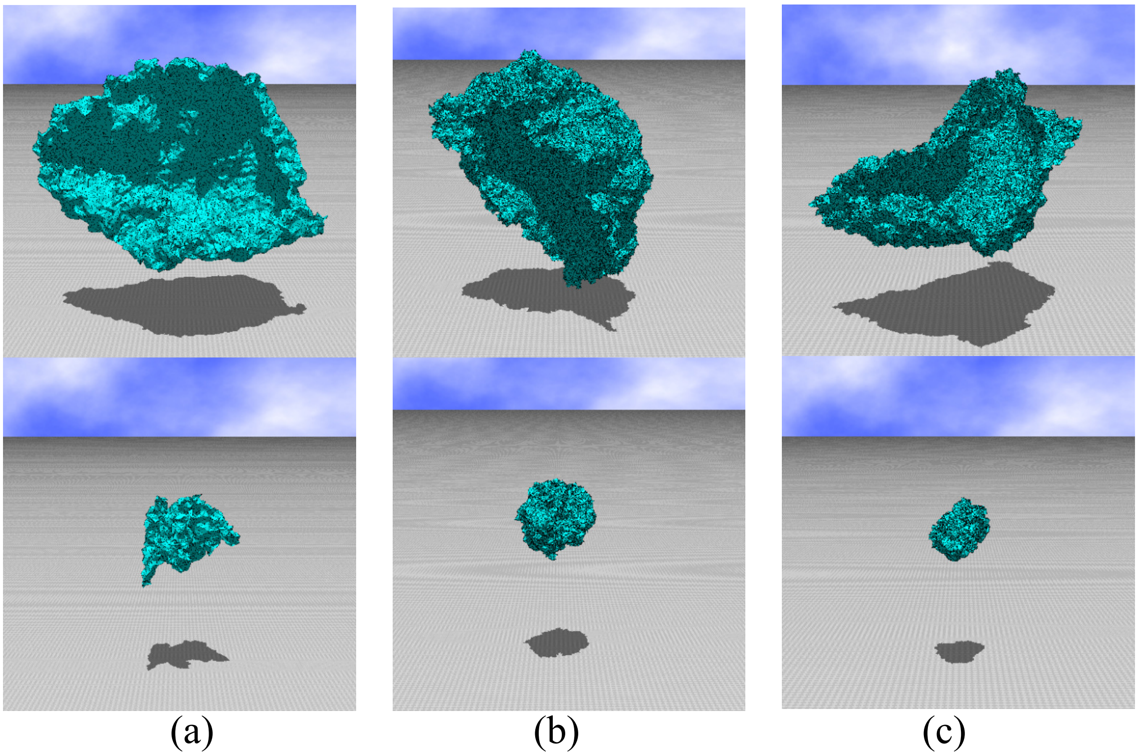

Figure 6. Snapshots of surfaces obtained in the replica $i(\in\{1,\cdots,N_R\})$ such that $i=N_R(=24)$ in the upper low and $i=1$ in the lower low, which correspond to the flat phase and the crumpled phase, respectively, in each model. The models and lattice size N are (a) LG, $N=7351$, (b) canonical, $N=44287$, and (c) modified canonical, $N=20917$.

given as follows: (a) $\kappa=0.1835$ (upper), $\kappa=0.187$ (lower), (b) $\kappa=0.766$ (upper), $\kappa=0.782$ (lower), and (c) $\kappa=0.451$ (upper), $\kappa=0.467$ (lower). In the LG model simulations, the parameters (t,u,v) are fixed to

$$(t,u,v)=(-6,0.2,0.2),\quad (\mathrm{LG}). \tag{19}$$

We find that the surfaces in the upper low are globally bending but almost flat while those in the lower low shrink to a small ball. From this observation, we understand that the surfaces in the upper and lower lows are in the flat and crumpled phases, respectively, in all of the models.

3.2. Bending energy and mean square gyration

The bending energy of the LG model is calculated only on the internal vertices, because the definition of S_2 on the boundary vertices is slightly different from that on the internal vertices as described in Section 2.2. In Figs. 7(a)– 7(i), we plot the bending energy S_2/N_B of the LG model and the other models, the specific heat

$$C_{S_2}=\frac{\kappa^2}{N}\left\langle\left(S_2-\langle S_2\rangle\right)^2\right\rangle, \tag{20}$$

and the peak $C_{S_2}^{\max}$ of the specific heat. We should note that N_B is the total number of internal bonds $N_B=3(N-6L)$ for the LG model, where $N-6L$ is the total number of internal vertices and hence $3(N-6L)$ is the total number of the diagonal lines such as 2′12 in Fig. 2(b). The reason why this N_B is used for S_2 in the LG model is because the first term of S_2 in Eq. (3) is defined on such diagonal lines, and the second term is also defined on a pair of diagonal lines 2′12 and 3′13 in Fig. 2(b), and there are three different such diagonal-lines on each internal vertex. For the other two models, $N_B(=N_E-6L)$ is

Peer-reviewed version available at *Polymers* **2018**, *10*, 1360; doi:10.3390/polym10121360

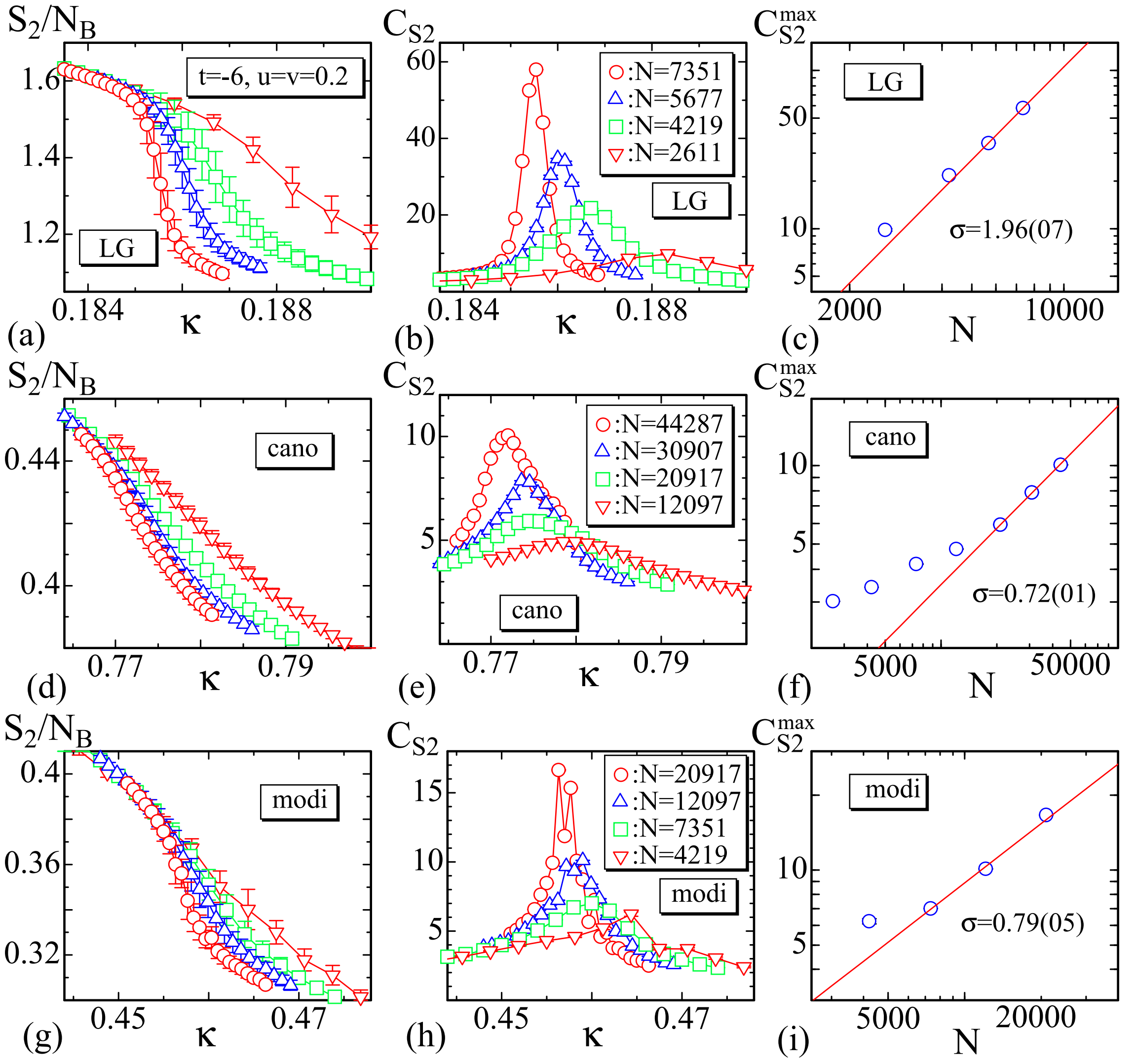

Figure 7. The bending energy per bond S_1/N_B, the specific heat C_{S_2}, and the log-log plot of the peak value $C_{S_2}^{\rm max}$ vs. N for (a),(b),(c) LG model, (a),(b),(c) canonical model, and (a),(b),(c) modified canonical model.

the total number of internal bonds, on which the bending energy S_2 is defined, where N_E is the total number of edges N_E given in Section 2.1. Note that C_{S_2} in Eq. (24) for the LG model is defined also by using N. The curves of C_{S_2} in Fig. 7(h) for the modified model are fluctuating, and this fluctuation may be due to the fact that the total number of iteration is not sufficient for this model as mentioned above, though reasonable peak values $C_{S_2}^{\rm max}$ are obtained.

From the LG model data plotted in Figs. 7(a)-7(c), we see that the S_2/N_B abruptly changes against κ, and correspondingly the C_{S_2} has the anomalous peak showing the existence of the crumpling transition. As mentioned above, the parameters (t, u, v) are fixed to the values in Eq. (19) and remain unchanged. The peak heights $C_{S_2}^{\rm max}$ vs. N are plotted in log-log scale in Figs. 7(c), where N is used. The data obtained by the other models are also plotted in Figs. 7(d)-7(f) and Figs. 7(g)-7(i). Fitting the largest three data of $C_{S_2}^{\rm max}$ to the scaling relation

$$C_{S_2}^{\rm max} \sim N^{\sigma}, \tag{21}$$

Peer-reviewed version available at Polymers 2018, 10, 1360; doi:10.3390/polym10121360

we have

$$\sigma = 1.96 \pm 0.07 \ (\mathrm{LG}), \quad \sigma = 0.72 \pm 0.01 \ (\mathrm{cano}), \quad \sigma = 0.79 \pm 0.05 \ (\mathrm{modi}). \tag{22}$$

We find from these results that the transition of the LG model is of first-order while in the other two models the transition is of second-order, because $\sigma \geq 1$ in the LG model and $\sigma < 1$ in the other models. The first result in Eq. (22) of the LG model is qualitatively comparable to $\sigma = 1.58 \pm 0.08$ of the canonical model on spherical lattice in Ref. [28], because both results indicate that the transition is of first-order. In contrast, the latter two results in Eq. (22) of the other models indicate the second-order transition, and hence these two are completely different from the result in Ref. [28]. We consider that this difference simply comes from the difference in the lattice topology or structure; sphere and disk, which are surfaces without a boundary and with a free boundary, or are compact and non-compact.

We calculate the coefficient σ in Eq. (21) for the LG model using the specific heat C_{S_2} of the bending energy S_2 in Eq. (12), and we have $\sigma = 1.96 \pm 0.07$, which is almost identical to the first result $\sigma = 1.97 \pm 0.07$ in Eq. (22). This indicates that the results $\sigma = 1.96 \pm 0.07$ in Eq. (22) for the LG model is reliable, although this result is obtained from the bending energy on the internal vertices only.

The problem here is ascertaining why the result of LG model in Eq. (22) is different from the others. Firstly, we should be reminded that it is predicted that the LG model has a continuous crumpling or wrinkling transition from the mean filed analysis [11]. However, as mentioned in Ref. [28], the basic assumption for the mean field analysis that the surface fluctuation is relatively small is not always true even for the models. This is considered to be the reason why the result of the LG model deviates from the mean field prediction and has the first-order transition even on the lattice with a free boundary. Next, we have to consider from where comes the difference in the order of transitions between the LG model and the other two models. One possible origin is the shear stress or resistance to shear deformation expected in the LG model; it is not expected in the other models. The bending energy S_2 assumed in the LG models is identical to S_2 in the other models up to a numerical factor, and this S_2 has no shear resistance to in-plane deformation of triangles; it has only a resistance to the bending or out-of-plane deformation. Thus, the only source for the shear resistance is the Gaussian bond potential S_1 in the two models, while in the LG model, S_3 and S_4 as well as S_1 have resistance to shear stresses. Here, we should note that all models are fixed-connectivity or tethered models, and the shear resistance is not negligible compared to the fluid surface models on dynamically triangulated lattices. In the tethered models, any deformations of triangles except simple expansion/shrinkage accompany a shear resistance, because all triangles tend to become regular in the equilibrium configurations. Note that the simple expansion and shrinkage of triangles are suppressed because the mean bond length remains constant due to the scale invariant property of the partition function.

The mean square radius of gyration R_g^2 defined by

$$R_g^2 = \frac{1}{N}\sum_i \left(\mathbf{r}_i - \bar{\mathbf{r}}\right)^2, \quad \bar{\mathbf{r}} = \frac{1}{N}\sum_i \mathbf{r}_i, \tag{23}$$

its variance

$$C_{R_g} = \frac{1}{N}\left\langle \left(R_g^2 - \langle R_g^2\rangle\right)^2 \right\rangle, \tag{24}$$

and the peak values $C_{R_g}^{\max}$ are plotted in Figs. 8(a)–8(i). The fluctuations of the data C_{R_g} in Fig. 8(h) are relatively large due to the same reason for C_{S_2} mentioned above. We also find that R_g^2 rapidly changes, where C_{R_g} has a peak $C_{R_g}^{\max}$. The peak position on the κ axis for $C_{R_g}^{\max}$ of the LG model is almost identical with the position for $C_{S_2}^{\max}$, while those for $C_{R_g}^{\max}$ and $C_{S_2}^{\max}$ in the other models are considerably different from each other. This difference is not observed in the canonical model on spherical lattice in Ref. [28], where a first-order transition is expected and where the transition point is

Peer-reviewed version available at Polymers 2018, 10, 1360; doi:10.3390/polym10121360

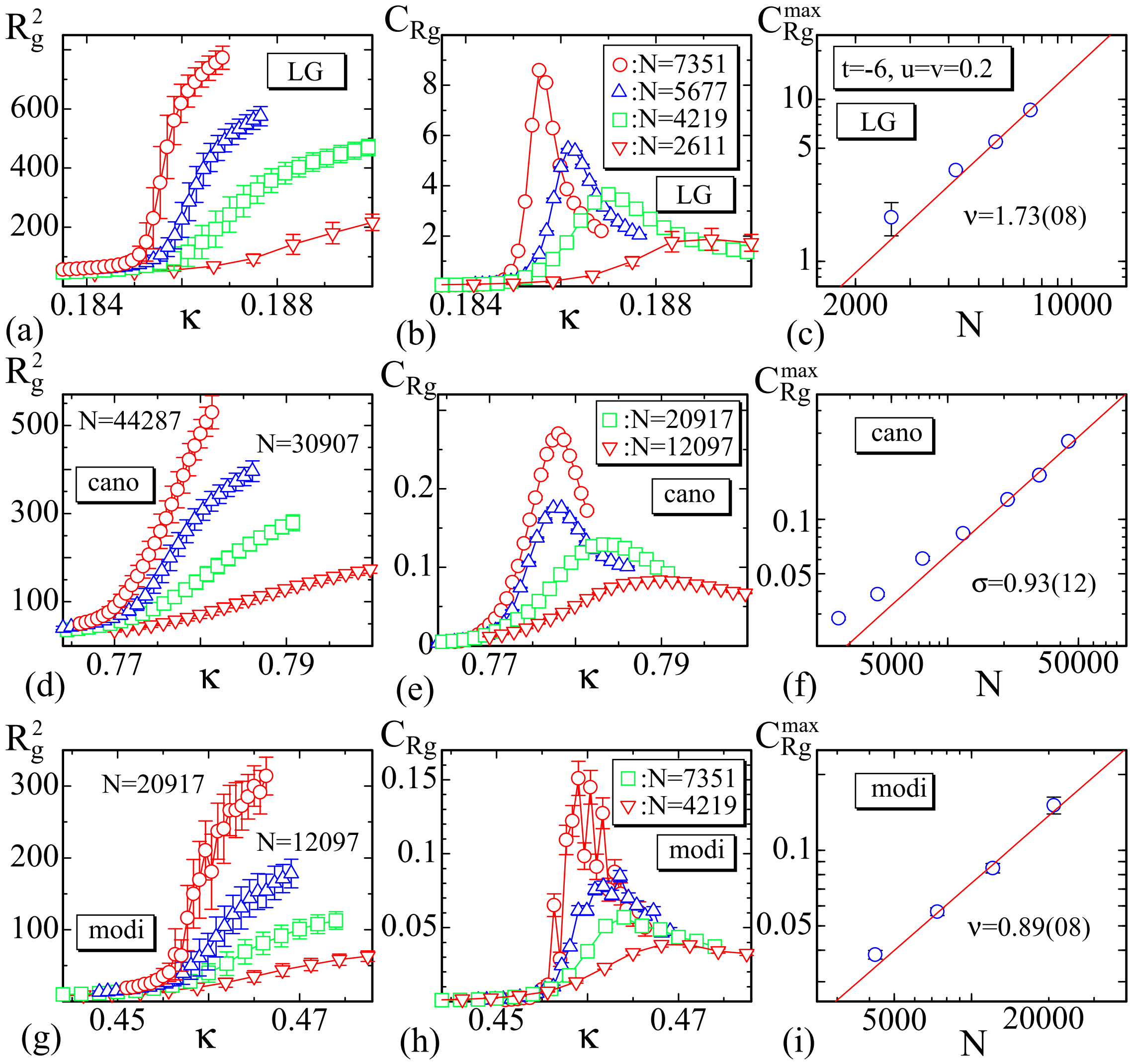

Figure 8. The mean square gyration R_g^2, its variance C_{R_g}, and the log-log plot of the peak value $C_{R_g}^{\max}$ vs. N for (a),(b),(c) LG model, (d),(e),(f) canonical model, and (g),(h),(i) modified canonical model.

very clear and detected uniquely even by numerical simulations. In contrast, continuous transitions are relatively unclear in general, and hence the transition points of the latter two models are relatively hard to observe. Moreover, the total number of iterations for these are not always sufficiently large as mentioned above. These are possible reasons for the deviation of the transition points observed in $C_{R_g}^{\max}$ and $C_{S_2}^{\max}$.

The peak values $C_{R_g}^{\max}$ are expected to scale according to

$$C_{R_g}^{\max} \sim N^{\mu}. \tag{25}$$

By fitting the largest three data of $C_{R_g}^{\max}$ in Figs. 8(c), 8(f) and 8(i) to this relation, we have

$$\mu = 1.73 \pm 0.08 \ (\text{LG}), \quad \mu = 0.93 \pm 0.12 \ (\text{cano}), \quad \mu = 0.89 \pm 0.08 \ (\text{modi}). \tag{26}$$

These results also support the proposition that the LG model has a first-order transition and the other models a second-order transition, though the coefficient of the canonical model is close to $\mu = 1$ and the transition is close to a first-order one. The reason why μ in Eq. (26) of the LG model is $\mu > 1$ may be the

Peer-reviewed version available at Polymers 2018, 10, 1360; doi:10.3390/polym10121360

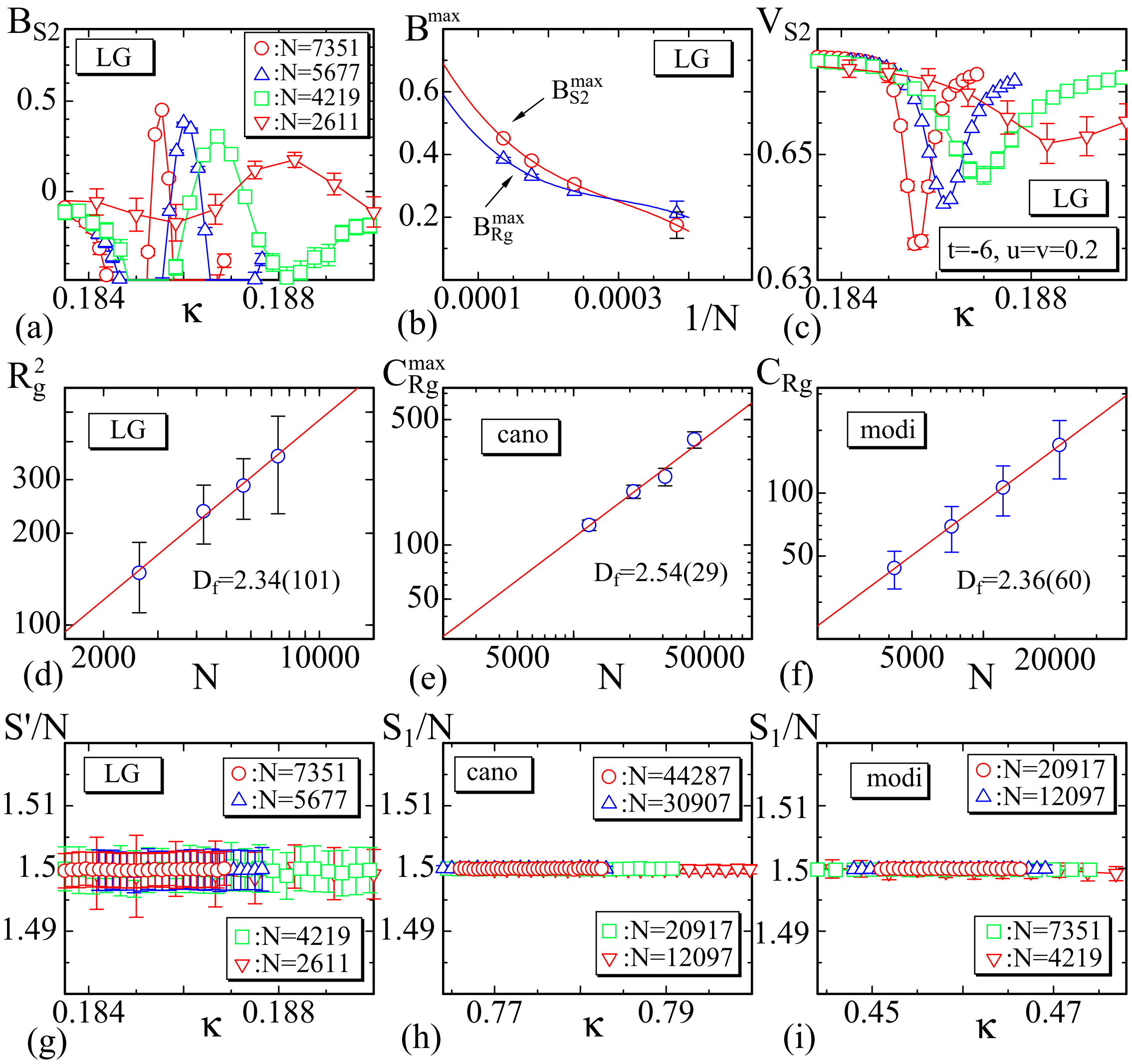

Figure 9. (a) The Binder quantity B_{S_2}, (b) the peak values $B^{\max}_{S_2}$ and $B^{\max}_{R_g}$ vs $1/N$ with solid lines drawn by Mathematica command "Interpolation", and (c) the Binder cumulant V_{S_2} for the LG model. The log-log plot of R_g^2 vs. N of (a) the LG model, (b) the canonical model, and (c) the modified canonical model. (g) S' of the LG model, and S_1/N of (b) the canonical model and (c) the modified canonical model.

fact that the surface is not self-avoiding [28]. We should note that the order of transition depends on its definition. If we call a transition first-order only if the coefficient μ for the variance CS_* of Hamiltonian S_* is $\mu=1$, then the canonical and modified models clearly have a second-order transition from the results σ in Eq. (22). In general, the coefficient σ for the bending energy S_2 is more important than μ as a coefficient for the determination of the order of transition. Thus, it is reasonable to consider that the crumpling transitions of the canonical and modified canonical models are continuous transitions.

3.3. Binder quantity and fractal dimension

Firstly. in this subsection, we calculate the Binder quantity B_{S_2} defined by [52,53]

$$B_{S_2}=1-\frac{\left\langle (S_2-\langle S_2\rangle)^4\right\rangle}{3\left\langle (S_2-\langle S_2\rangle)^2\right\rangle^2} \tag{27}$$

Peer-reviewed version available at *Polymers* **2018**, *10*, 1360; doi:10.3390/polym10121360

for the LG model (Fig. 9(a)). It is expected that B_{S_2} has a peak $B_{S_2}^{\rm max}$ and $B_{S_2}^{\rm max}\to 2/3$ at the first order transition point. To see whether this expectation is satisfied or not, $B_{S_2}^{\rm max}$ vs. $1/N$ are plotted in Fig. 9(b), where the Binder quantity $B_{R_g}^{\rm max}$ for R_g^2 is also plotted. The solid lines are also drawn by Mathematica command "Interpolation" for the data of $B_{S_2}^{\rm max}$ and $B_{R_g}^{\rm max}$. The value $B_{S_2}^{\rm max}(N\to\infty)$ on the vertical axis expected from the extrapolations is almost identical with $2/3$, while $B_{R_g}^{\rm max}(N\to\infty)$ is slightly smaller than $2/3$. This deviation of $B_{R_g}^{\rm max}(N\to\infty)$ seems due to the size effect, because the lattice size is not so large compared to those used in Ref. [28], where $B_{S_2}^{\rm max}(N\to\infty)\simeq 0.7$ and $B_{R_g}^{\rm max}(N\to\infty)\simeq 0.69$ are observed.

A first-order transition is also reflected in the Binder cumulant V_{S_2}, which is defined by [52,53]

$$V_{S_2}=1-\left\langle S_2^4\right\rangle/\left(3\langle S_2^2\rangle^2\right). \tag{28}$$

The Binder cumulant V_{R_g} for R_g^2 is also defined analogously to Eq. (28). These quantities are expected to have the minimum $V_{S_2}^{\rm min}$ and $V_{R_g}^{\rm min}$ at the first-order transition point, and this expectation is confirmed in Fig. 9(c), where only $V_{S_2}^{\rm min}$ is plotted. It is also found that the position of $V_{S_2}^{\rm min}$ on the κ axis is almost the same as that of $C_{S_2}^{\rm max}$ in Fig. 7(b). This also implies that $V_{S_2}^{\rm min}$ reflects the first-order transition.

In the other two models, the quantities B_{S_2} and V_{S_2} (and those for R_g^2) are unclear compared to the case of LG model. One of the reasons for this is the continuous nature of the transition; the convergent speed of the simulation is very slow close to the transition point.

Next, we calculate the fractal dimension D_f, which is defined by

$$R_g^2\sim N^{2/D_f}. \tag{29}$$

To calculate this quantity at the transition point, we plot R_g^2 vs. N in Figs. 9(d) - 9(f) in the log-log scale, where R_g^2 are obtained at the peak position of C_{R_g} in Figs. 8(b), 8(e) and 8(h). By fitting the plotted data to Eq. (29), we obtain

$$D_f=2.34\pm1.01\;({\rm LG}),\quad D_f=2.54\pm0.29\;({\rm cano}),\quad D_f=2.36\pm0.60\;({\rm modi}). \tag{30}$$

Since the errors of R_g^2 are large in the first and third models (see Figs. 9(d) and 9(f)), the errors in D_f are also relatively large. The values of D_f within these errors are comparable to $D_f=2.50\pm0.30$ at the first-order transition point of the canonical model on the spherical lattice in Ref. [28].

To check the simulations are performed correctly, we can use the relations

$$\begin{aligned} &S_1'/N=3/2\quad ({\rm LG}),\\ &S_1/N=3/2\quad ({\rm cano,\ modi}), \end{aligned} \tag{31}$$

where S_1' of the first one is given in Eq. (7), and $S_1'=tS_1+\kappa S_2+2uS_3+2vS_4$. The second equality is also obtained by using almost the same technique for the first one. The symbol $\langle\cdot\rangle$ is omitted for these S_1' and S_1 for simplicity. The results plotted in Figs. 9(g) – 9(i) are consistent with these predictions in Eq. (31).

4. Summary and Conclusion

In this paper, we study the crumpling transition of a planar surface with a free boundary by parallel tempering Monte Carlo (PTMC) simulations using three different tethered lattice models; the Landau-Ginzburg (LG) model, the canonical (cano) model, and the modified canonical (modi) model, defined on triangulated fixed-connectivity lattices of disk topology. The order of the transition is first-order in the LG model, while it is of second-order in the other models. This second-order nature of the transition is consistent with the result reported in [22,23].

Peer-reviewed version available at Polymers 2018, 10, 1360; doi:10.3390/polym10121360

The models studied in this paper are not self-avoiding, however, the transition between the crumpled and smooth phases indicates that these states are stable against thermal fluctuations. This can give insights into studies on real materials such as graphene, where the crumpled states are expected to have many technological applications.

In the presence of impurity, a new phase is expected to appear, and the surface critical exponents are also expected to change from those of the model without impurity [54]. Thus, it is interesting to study the planer surface model with impurities.

Acknowledgments: The author H.K. acknowledges D. Mouhanna and J.P. Kownacki for discussions. This work is supported in part by JSPS KAKENHI Grant Number JP17K05149.

Author Contributions: A.S. performed planning and modeling and evaluated the simulation results; H.K. performed planning, modeling and simulations and wrote the paper.

Conflicts of Interest: The authors declare no conflict of interest.

Abbreviations

The following abbreviations are used in this manuscript:

MC	Monte Carlo
PTMC	parallel tempering Monte Carlo
MMC	Metropolis Monte Carlo
MCS	Monte Carlo sweeps
LG	Landau Ginzburg
cano	canonical
modi	modified canonical

References

1. Helfrich, W. Elastic Properties of Lipid Bilayers: Theory and Possible Experiments. *Z. Naturforsch C.* **1973**, *28*, 693-703.
2. Polyakov, A.M. Fine structure of strings. *Nucl. Phys. B.* **1986**, *268*, 406-412.
3. Peliti, L.; Leibler, S. Effects of Thermal Fluctuations on Systems with Small Surface Tension. *Phys. Rev. Lett.* **1985**, *54*, 1690-1693.
4. Guitter E.; David F.; Leibler, S.; Peliti, L. Crumpling and Buckling Transitions in Polymerized Membranes. *Phys. Rev. Lett.* **1988**, *61*, 2949-2952.
5. David, F.; Guitter, E. Crumpling Transition in Elastic Membranes: Renormalization Group Treatment. *Europhys. Lett.* **1988**, *5*, 709-714.
6. Nelson D. The Statistical Mechanics of Membranes and Interfaces. In *Statistical Mechanics of Membranes and Surfaces, Second Edition*. Nelson, D.; Piran, T.; Weinberg, S., Eds., World Scientific: Singapore, 2004; pp.1-17.
7. Wheater, J.F. Random surfaces: from polymer membranes to strings. *J. Phys. A Math. Gen.* **1994**, *27*, 3323-3354.
8. Kownacki, J.-P.; Mouhanna, D. Crumpling transition and flat phase of polymerized phantom membranes. *Phys. Rev. E* **2009**, *79*, 040101(R).
9. Essafi, K.; Kownacki, J.P.; Mouhanna, D. First-order phase transitions in polymerized phantom membranes. *Phys. Rev. E* **2014**, *89*, 042101(1-5).
10. Bowick ,M.; Travesset, A. The statistical mechanics of membranes. *Phys. Rep.* **2001**, *344*, 255-308.
11. Bowick, M.J. Fixed-connectivity Membranes. In *Statistical Mechanics of Membranes and Surfaces, Second Edition*. Nelson, D.; Piran, T.; Weinberg, S., Eds., World Scientific: Singapore, 2004; pp.323-357.
12. Gompper, G.; Kroll, D.M. Triangulated-surface Models of Fluctuating Membranes. In *Statistical Mechanics of Membranes and Surfaces, Second Edition*. Nelson, D.; Piran, T.; Weinberg, S., Eds., World Scientific: Singapore, 2004; pp.359-426.
13. Kantor, Y.; Karder, M.; Nelson, D.R. Tethered surfaces: Statics and dynamics. *Phys. Rev. A.* **1987**, *35*, 3056-3071.

Peer-reviewed version available at *Polymers* **2018**, *10*, 1360; doi:10.3390/polym10121360

14. Kantor, Y.; Nelson, D.R. Phase Transitions in Flexible Polymeric Surfaces. *Phys. Rev. A*. **1987**, *36*, 4020-4032.
15. Ho, J.-S.; Baumgärtner, A. Simulations of Fluid Self-Avoiding Membranes. *Europhys. Lett.* **1990**, *12*, 295–300.
16. Ambjörn, J.; Irbäck, A.; Jurkiewicz, J.; Petersson, B. The theory of dynamical random surfaces with extrinsic curvature. *Nucl. Phys. B* **1993**, *393*, 571–600.
17. Kownacki, J-P.; Diep, H.T. First-order transition of tethered membranes in three-dimensional space. *Phys. Rev. E*. **2002**, *66*, 066105(1-5).
18. Nishiyama, Y. Crumpling transition of the triangular lattice without open edges: Effect of a modified folding rule. *Phys. Rev. E*. **2010**, *81*, 041116(1-6).
19. Nishiyama, Y. Crumpling transition of the discrete planar folding in the negative-bending-rigidity regime. *Phys. Rev. E*. **2010**, *82*, 012102(1-64).
20. Koibuchi, H.; Endo, E. First-order phase transition of the tethered membrane model on spherical surfaces. *Nucl. Phys. B [FS]*. **2006**, *732*, 11-16.
21. Igawa, M.; Koibuchi, H.; Yamada, M. Monte Carlo simulations of a tethered membrane model on a disk with intrinsic curvature . *Phys. Lett. A*. **2005**, *338*, 433-438.
22. Bowick, M.J.; Catterall, S.M.; Falcioni, M.; Thorleifsson, G.; Anagnostopoulos, K.N. The Flat Phase of Crystalline Membranes. *J. Phys. I France*. **1996**, *6*, 1321-1345.
23. Cuerno,R.; Caballero, R.G.; Gordillo-Guerrero, A.; Monroy, P.; Ruiz-Lorenzo, J.J. Universal behavior of crystalline membranes: Crumpling transition and Poisson ratio of the flat phase. *Phys. Rev. E*. **2016**, *93*, 022111(1-9).
24. Hukushima, K.; Nemoto, K. Exchange Monte Carlo method and application to spin glass simulations. *J. Phys. Soc. Jpn*. **1996**, *65*, 1604–1608.
25. Takayama, H.; Hukushima, K. Computational experiment on glassy dynamic nature of field-cooled magnetization in ising spin-glass model. J. Phys. *Soc. Jpn*. **2007**, *76*, 013702(1–4).
26. Neuhaus, T.; Magiera, M.P.; Hansmann, U.H.E. Efficient parallel tempering for first-order phase transitions. *Phys. Rev. E*. **2007**, *76*, 045701R(1–4).
27. Fiore, C.E. First-order phase transitions: a study through the parallel tempering method. *Phys. Rev. E*. **2008**, *78*, 041109(1–5).
28. Usui, S.; Koibuchi, H. Parallel TemperingMonte Carlo Simulations of Spherical Fixed-Connectivity Model for Polymerized Membranes. *J. Stat. Phys*. **2016**, *162*, 701-711.
29. Koltonow, A.R.; Luo, C.; Luo,J.; Huang, J. Graphene Oxide Sheets in Solvents: To Crumple or Not To Crumple?. *ACS Omega*. **2017**, *2*, 18005-8009.
30. Shang, J.; Chen, Y.; Zhou, Y.; Liu, L.; Wang, G.; Li, X.; Kuang, J.; Liu, Q.; Dai, Z.; Miao, H.; Zhi, L.; Zhang, Z. Effect of folded and crumpled morphologies of graphene oxide platelets on the mechanical performances of polymer nanocomposites. *Polymer*. **2014**, *68*, 131-139.
31. Novoselov, K.S.; Geim, A.K.; Morozov, S.V.; Jiang, D.; Zhang, Y.; Dubonos, S.V.; Grigorieva, I.V.; Firsov, A.A. Electric Field Effect in Atomically Thin Carbon Films. *Science*. **2004**, *306 (5696)*, 666-669.
32. Novoselov, K.S.; Jiang, D.; Schedin, F.; Booth, T.J.; Khotkevich, V.V.; Morozov, S.V.; Geim, A.K. Two-dimensional atomic crystals. *PNAS*. **2005**, *102*, 10451–10453.
33. Deng, S.; Berry, V. Wrinkled, rippled and crumpled graphene: an overview of formation mechanism, electronic properties, and applications. *Materials Today*. **2016**, *19*, 197-212.
34. Papageorgiou, D.G.; Kinloch, I.A.; Young, R.J. Mechanical properties of graphene and graphene-based nanocomposites. *Prog. Mat. Sci.*. **2017**, *90*, 75-127.
35. Zang, J.; Ryu, S.; Pugno, N.; Wang, Q.; Tu, Q.; Buehler, M.J.; Zhao, X. Multifunctionality and control of the crumpling and unfolding of large-area graphene. *Nature Mat*. **2013**, 3542(1-5), DOI: 10.1038/NMAT3542.
36. Luo, J.; Jang, H.D.; Sun, T.; Xiao, L.; He, Z.; Katsoulidis, A.P.; Kanatzidis, M.G.; Gibson, J.M.; Huang, J. Compression and Aggregation-Resistant Particles of Crumpled Soft Sheets. *ACS Nano*. **2011**, *5(11)*, 8943-8949.
37. Chee, W.K.; Lim, H. N.; Huang, N.M., Harrison, I. Nanocomposites of Graphene/ Polymers: A Review. *RSC Advances*. **2015**,*5*, 68014-68051.
38. Díez-Pascual, A.M.; Sánchez, J.A.L.; Capilla, R.P.; Díaz, P.G. Recent Developments in Graphene/Polymer Nanocomposites for pplication in Polymer Solar Cells. *Polymers*. **2018**,*10*, 217(1-22).
39. Kim, H.; Abdala, A.A.; Macosko C.W. Graphene/Polymer Nanocomposites. *Macromolecules*. **2010**,*43*, 6515–6530.

Peer-reviewed version available at *Polymers* **2018**, *10*, 1360; doi:10.3390/polym10121360

40. Dai, Z.; Weng, C.; Liu, L.; Hou, Y.; Zhao, X.; Kuang, J.; Shi, J.; Wei, Y.; Lou, J.; Zhang, Z. Multifunctional Polymer-Based Graphene Foams with Buckled Structure and Negative Poisson's Ratio. *Scientific Reports*. **2016**, *6*, 32989(1-9).
41. Marsden, A.J.; Papageorgiou, D.G.; Vallés, C.; Liscio, A.; V Palermo, V.; Bisse, M.A.; Young, R.J.; Kinloch, I.A. Electrical percolation in graphene–polymer composites. *2D Mater*. **2018**, *5*, 032003(1-19).
42. Creutz, M. *Quarks, gluons and lattices*. Cambridge University Press: Cambridge, United Kingdom,1983.
43. Paczuski M., Kardar M. and Nelson D.R. Landau Theory of the Crumpling Transition. *Phys. Rev. Lett.* **1988**, *60*, 2638-2640.
44. Koibuchi, H.; Shobukhov, A. Monte Carlo simulations of Landau-Ginzburg model for membranes . *Int. J. Mod. Phys. C*. **2014**, *25*, 1450033(1-18).
45. Koibuchi, H. Monte Carlo studies of triangulated spherical surfaces in the two-dimensional space . *Nucl. Phys. B [FS]*. **2010**, *836*, 186-203.
46. Ueno, K. Algebraic geometry and string theory (in Japanese) . In *Developments in mathematical physics (in Japanese)*. Ezawa, H; Kojima, I., Eds.; Tokyo Tosho: Tokyo, Japan, 1988: pp.111-149.
47. Doi, M.; Edwards, S.F. *The Theory of Polymer Dynamics*. Oxford University Press: Oxford, United Kingdom, 1986.
48. Koibuchi, H.; Sekino, H. Monte Carlo studies of a Finsler geometric surface model. *Physica A*. **2014**, *393*, 37-50.
49. Proutorov, E.; Matsuyama, N.; Koibuchi, H. Finsler geometry modeling and Monte Carlo study of liquid crystal elastomer under electric fields. *J. Phys: Condens. Matter*. **2018**, *30*, 405101(1-13).
50. Metropolis, N.; Rosenbluth, A.W.; Rosenbluth, M.N.; Teller, A.H. Equation of State Calculations by Fast Computing Machines. *J. Chem. Phys.* **1953**, *21*, 1087-1092.
51. Landau, D.P. Finite-size behavior of the Ising square lattice. *Phys. Rev. B*. **1976**, *13*, 2997-3011.
52. Binder, K. Finite size scaling analysis of ising model block distribution functions. *Z. Phys. B*. **1981**, *43*, 119–140.
53. Challa, M.S.S.; Landau, D.P.; Binder, K. Finite-size effects at temperature-driven first-order transitions. *Phys. Rev. B*. **1986**, *34*, 1841–1852.
54. Coquand, O; Essafi, K.; Kownacki, J.-P.; Mouhanna, D. Glassy phase in quenched disordered crystalline membranes. *Phys. Rev. E*. **2017**, *97*, 030102(R)(1-5).